Article

Surgical Staplers in Laparoscopic Colectomy: A New Innovative Flexible Design Perspective [†]

Dhruva Khanzode [1,2,‡] , **Ranjan Jha** [1,2,‡] , **Alexandra Thomieres** [3,‡] , **Emilie Duchalais** [3,‡]
and Damien Chablat [4,5,*,‡]

1   CSIR-Central Scientific Instruments Organisation, Chandigarh 160030, India;
    dhruva.csio20a@acsir.res.in (D.K.); ranjan.jha@csio.res.in (R.J.)
2   Academy of Scientific and Innovative Research (AcSIR), Ghaziabad 201002, India
3   Centre Hospitalier Universitaire, F-44000 Nantes, France; alexandra.thomieres@chu-nantes.fr (A.T.);
    emilie.dassonneville@chu-nantes.fr (E.D.)
4   École Centrale Nantes, Nantes Université, CNRS, LS2N, UMR 6004, F-44000 Nantes, France
5   Research Center for Industrial Robots Simulation and Testing, Technical University of Cluj-Napoca,
    400114 Cluj-Napoca, Romania
*   Correspondence: damien.chablat@cnrs.fr
†   This paper is an extended version of our paper published in Khanzode, D., Jha, R., Thomieres, A.; et al.
    Design of a Surgical Stapler for Laparoscopic Colectomy. In Proceedings of the New Trends in Medical and
    Service Robotics (MESROB 2023), Craiova, Romania, 7–10 June 2023; pp. 71–80.
‡   These authors contributed equally to this work.

Abstract: This article describes the development of a flexible surgical stapler mechanism, which serves as a fundamental tool for laparoscopic rectal cancer surgery, addressing the challenges posed by difficult types of accessibility using conventional instruments. The design of this mechanism involves the incorporation of a stacked tensegrity structure, in which a flexible beam serves as the central spine. To assess the stapler's range of operation, an analysis of the workspace was conducted by examining collaborative Computed Tomography (CT) scan data obtained from different perspectives (Axial, Coronal, and Sagittal planes) at various intervals. By synthesizing kinematic equations, Hooke's law was employed, taking into account rotational springs and bending moments. This allowed for precise control of the mechanism's movements during surgical procedures in the rectal region. Additionally, the study examined the singularities and simulations of the tensegrity mechanism, considering the influential eyelet friction parameter. Notably, the research revealed that this friction parameter can alter the mechanism's curvature, underscoring the importance of accurate analysis. To establish a correlation between the virtual and physical models, a preliminary design was presented, facilitating the identification of the friction parameter.

Keywords: surgical stapler; anastomosis; laparoscopy; tensegrity mechanism

1. Introduction

Over the last two decades, significant advancements have been achieved in medical science. Surgical procedures that were once difficult, risky, and painful, such as open-heart surgeries, now have safer alternatives. Endoscopies and catheterization procedures have become mainstream, replacing the need for extensive open surgeries. Minimally invasive surgical techniques have also gained popularity, becoming the preferred choice for many traditional surgeries. These procedures involve small incisions on the body, through which specialized slender instruments with miniature tools are inserted. These tiny instruments have undergone modernization and are presently operated through robotic systems. Robotics is gaining increasing prominence across various domains within medical science, encompassing tasks such as diagnosis, drug administration, and therapy.

In surgical procedures, a frequent obstacle is the constrained room for maneuvering surgical instruments within the designated surgical area. To overcome this challenge,

the creation of innovative, compact surgical tools necessitates a thorough examination of the available workspace. Traditionally, computed tomography scans (CT scans) are employed for space assessment. CT scans utilize a blend of X-ray technology and computer processing to generate intricate visuals of the body's internal structures, encompassing bones, muscles, organs, and blood vessels. In comparison to conventional X-rays, CT scans offer a more comprehensive and precise dataset.

One common medical procedure is total mesorectal excision. It is used when there is rectal cancer or inflammation that requires removing part or all of the rectum. In this surgery, the upper part or the whole rectum is detached from the colon, and then the remaining parts (colon and lower rectum) are joined together. This connection of the colon and rectum is called colorectal anastomosis. A specialized surgical tool called a "surgical stapler" is used for colorectal anastomosis [1].

The emergence of the surgical stapler as a pivotal medical innovation can be traced back to 1908, when Victor Fischer and Hümér Hültl [2] introduced this groundbreaking device [3]. This instrumental apparatus emerged in response to the imperative of reducing the risk of wound contamination in abdominal surgeries by effectively containing gastrointestinal fluids. Initially referred to as a "mechanical stitching device" in academic literature [3], the Fischer–Hültl surgical stapler featured a design incorporating four rows of U-shaped staples constructed from steel wires, measuring 17 cm and 11 cm in length. Two enduring design features, the final B-shaped staple configuration [4], facilitating tissue perfusion, and the strategic staggered arrangement of staple pins [5], were integral aspects of this innovation.

The subsequent evolution of surgical staplers witnessed refinements and innovations throughout the 20th century, with researchers such as Aladár Petz and H. Friedrich making significant contributions, introducing innovations like the "L" shaped stapler. A pivotal milestone occurred in 1964 when Mark Ravitch, Leon Hirsch, and Felicien Steichen, under the United States Surgical Corporation (USSC), introduced the modern surgical stapler [3]. This innovation marked a paradigm shift with the introduction of disposable staple cartridges, fundamentally reshaping surgical stapling technology. USSC also pioneered the development of surgical staplers with circular stapling zones, leading to designations such as TA (Thoracoabdominal) and GIA (Gastrointestinal Anastomosis) becoming synonymous with surgical practice. Subsequent corporate developments had profound impacts on the trajectory of surgical stapling technology within the medical field [6].

In modern surgical practice, five main types of staplers are commonly used: TA (Thoraco-Abdominal), GIA (Gastro-Intestinal Anastomosis), Endo GIA (Endoscopic Gastro-Intestinal Anastomosis), EEA (End–End Anastomosis), and Skin Stapler. Notably, the TA stapler does not include an integrated cutting mechanism for tissues after stapling, which requires manual separation. On the other hand, the EEA stapler is known for its formation of circular staples [7], and the Skin Stapler is employed for closing surface wounds. The TA stapler is primarily utilized in veterinary surgical procedures [8]. In contrast, both GIA and Endo GIA staplers are extensively used in abdominal surgeries, with the latter specifically designed for minimally invasive surgical procedures [9,10].

At present, Endo GIA staplers come in three distinct configurations: Passive Articulated Wrist Type (PAW) [11], Active Articulated Wrist Type (AAW) [12], and Radial Reload Type Staplers (RR). The PAW version achieves wrist flexion by exerting pressure on the jaw against the abdominal wall. In contrast, the AAW model incorporates a lever mechanism to articulate the wrist into predetermined bending angles. The RR-type stapler, exclusively offered by Covidien Inc., Westmeath, Ireland , is highly esteemed for pulmonary surgeries [13]. Nonetheless, a notable drawback of the RR-type stapler is its need for a considerably larger incision for entry into the body, which may contradict the principles of "minimally invasive surgery" [14]. Consequently, there is a pressing need for a surgical stapler capable of accessing the surgical site through laparoscopic openings while preserving the functionality of an RR-type stapler within the body.

In response to the challenges associated with the positioning and maneuverability of endoscopic surgical staplers, this article delves into the design and development of a hyper-redundant flexible surgical stapler specifically tailored for laparoscopic procedures. This innovative stapler is meticulously engineered to provide adaptable orientation within intricate surgical sites, thereby enhancing the efficiency of tissue sealing and division when compared to conventional endoscopic surgical staplers. In summary, the realm of medical science has witnessed remarkable progress, resulting in safer and more effective surgical interventions. The adoption of minimally invasive techniques and the introduction of specialized surgical staplers have played pivotal roles in modern healthcare practices, contributing significantly to improved patient outcomes and expedited recovery periods.

This article explores the design and development of a highly adaptable, flexible surgical stapler tailored for laparoscopic procedures, as detailed in [15]. The primary objective is to address the challenges associated with positioning and manoeuvrability that conventional endoscopic surgical staplers, often encounter [16]. The envisioned stapler exhibits the capability to dynamically adjust its orientation within intricate surgical sites, consequently enhancing the efficiency of tissue sealing and cutting when compared to current endoscopic staplers.

The surgical stapler comprises four fundamental components: the upper jaw, lower jaw, stapling cartridge, and wrist, as depicted in Figure 1. For the flexible surgical stapler design discussed in this article, the upper and lower jaws are designed with a stacked tensegrity mechanism incorporated in the body structure, as shown in Figure 9 in section 4 of the article [17]. This design enables both jaws to flex within the same plane, with the bending of these jaws being controlled by the actuation of tendons integrated within the tensegrity mechanism.
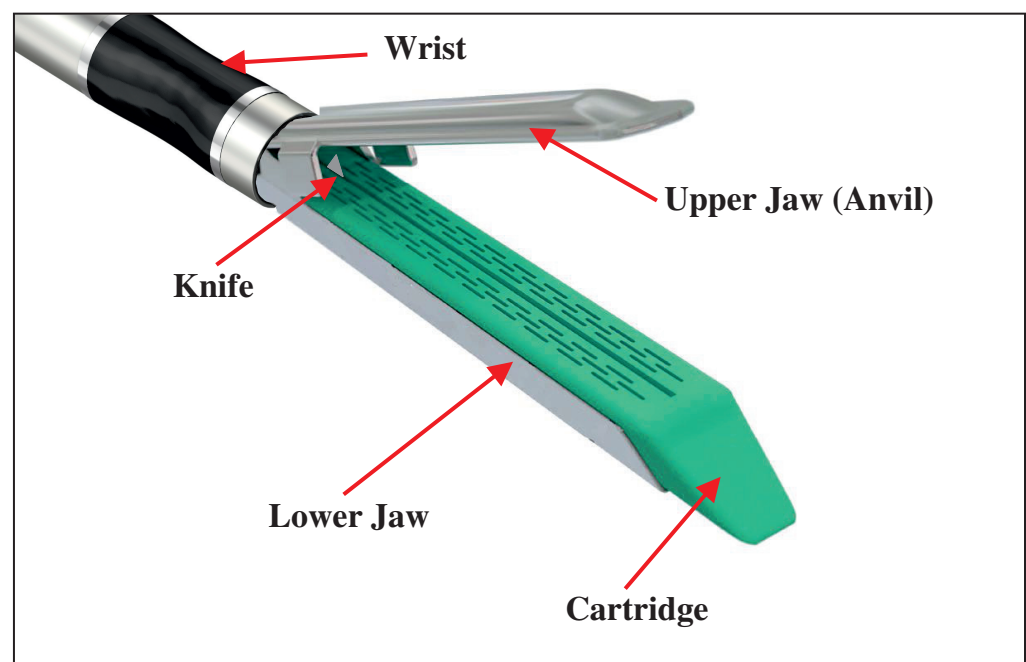
Figure 1. Various parts of a conventional endoscopic surgical stapler.

The stapling cartridge is intended to house surgical staple pins and a cutting knife, featuring a firing mechanism that engages the tissue and activates the knife simultaneously [18,19]. Additionally, the wrist, attached at the base of the jaw, is flexible and functions within the same plane as the upper and lower jaws, facilitated by the actuation of additional tendons. The mechanism responsible for articulating the upper and lower segments has been engineered as a decoupled system designed for application in the context of the jaw. The design is currently undergoing development to ensure the required force for securely closing the jaws while preventing potential tissue trauma.

To execute the full range of operations for the flexible surgical stapler, four distinct actuators come into play: one for bending the wrist, another for activating the staple pins and knife, a third for opening and closing the jaws, and finally, a unified actuation mechanism for synchronously bending the upper and lower jaws.

In [20], a simple kinematic model and its singular configurations were introduced for three segments in the simulation only. Extending from that, this article aims to discuss the design process of a multi-segmented mechanism utilizing CAD modeling, which integrates the results of mathematical modeling, kinematic simulations, and singularity analysis presented in the associated research for *n*-segments. The article also covers the prototyping of this design through SLA 3D printing and the subsequent dynamic experimentation conducted on the prototype.

2. Workspace Analysis

In the field of design and modeling, the first crucial step is to carefully examine the given problem statement and discern the inherent limitations and constraints that will shape the design process. When it comes to designing a flexible surgical stapler, the paramount constraint revolves around the available workspace. To formulate a practical design, it becomes imperative to delve into the stapler's potential maneuverability within the surgical environment. Frequently, this available space proves to be quite confined, presenting significant challenges for the efficient navigation of surgical instruments. Therefore, when crafting a novel, compact surgical tool, it becomes paramount to conduct an exhaustive analysis of the actual spatial allowances for the tool's mobility.

In this context, the standard approach involves the utilization of computed tomography (CT) scans to evaluate the accessible space. To conduct our analysis, we compiled data from a cohort of patients who had undergone colon surgery. The volume of the abdominal workspace is notably influenced by various factors, including the patient's age, gender, weight, and physiological attributes. To exemplify our research, we opted to focus on data obtained from a specific male patient, aged 65, with a height of 1.66 m and a weight of 55 kg. This particular patient was selected due to his unique physiological characteristics, which yielded the most confined workspace volume for the flexible surgical stapler

We then proceeded to acquire CT scan data for the general surgical site, encompassing three anatomical planes: Axial, Coronal, and Sagittal. These data points were spaced at 3.33-millimeter intervals for each plane. A skilled surgeon delineated the dimensional parameters of the surgical site on the data, denoted by red and blue markings in Figure 2, respectively, employing Vue PACS software, (version 12.1.6.1005, CARESTREAM Health, New York, NY, USA). Initially, these data underwent analysis to approximate the maximum workspace volume available for the flexible stapler. Subsequently, we pinpointed the most confined cross-sectional area within the surgical site, which came out to be 2613 mm^2 in the axial plane, 8036 mm^2 in the coronal plane and 6875 mm^2 in the sagittal plane.
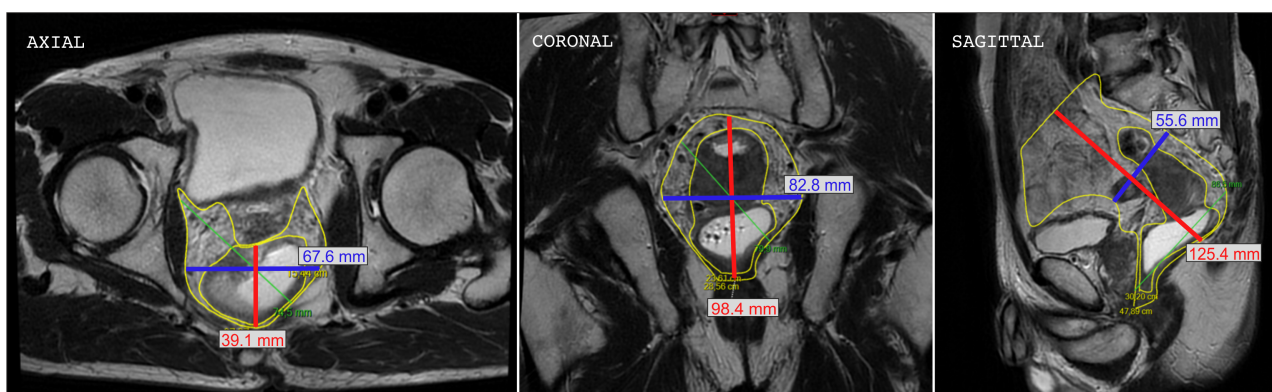
Figure 2. Sample CT scan data for workspace evaluation in Axial, Coronal, and Sagittal planes. The red and blue markings represent the available dimension (mm) in each plane.

Using this dataset, a three-dimensional model was crafted to simulate the placement of the stapler and its laparoscopic insertion. This simulation enables us to ascertain the optimal size of the tool that can be effectively utilized within the most restricted available space. By taking these factors into account, we can develop a surgical stapler capable of adeptly and precisely navigating challenging anatomical spaces during minimally invasive procedures.

3. Mechanism Design of Surgical Stapler

When dealing with a flexible mechanism, deformations or significant deflections often display nonlinear behavior. To streamline the process of kinematic modeling, the widespread practice is to employ the constant curvature technique. Constant curvature mechanisms consist of a finite number of curved segments, each characterized by a set of arc parameters that can be analytically transformed. The piece-wise constant curvature approximation (PCCA), as previously elucidated in research [21], provides a method for determining the direct kinematics of the mechanism. This method takes cable tension as input and yields the corresponding posture as output. Notably, the PCCA remains applicable even when a flexible mechanism possesses a singular flexible spine spanning all its segments [22]. This technique has proven its efficacy in a variety of flexible mechanisms, including those utilized in the realms of medical science and surgery.

In this article, our attention is directed toward a specific multi-segmented mechanism, which is arranged in a vertical stack as visually represented in Figure 3. This configuration embodies a novel formulation of the tensegrity mechanism detailed in [23]. A continuous flexible beam, allowing for in-plane deformation while preserving significant stiffness within that same plane (depicted in Figure 3), serves as the link connecting the base to the mobile platform of each segment. The continuous beam, denoted as $(A_1^0 A_n^0)$, stretches from the mechanism's base to its tip. To manipulate the shape of the mechanism, two cables are employed, extending from A_1^i to A_n^i and from A_1^j to A_n^j. Additionally, a set of springs is positioned along the cables to represent the elastic stress generated by the outer protective skin.
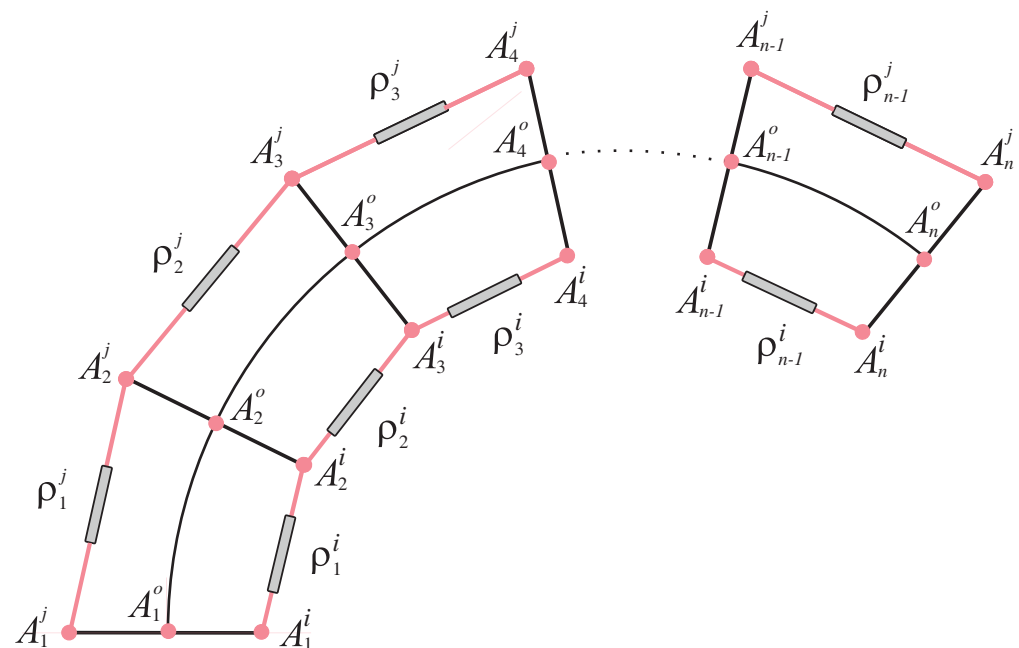
Figure 3. The tensegrity mechanism understudy with a stacked multi-segmented model with a flexible beam.

For analysis, our focus centres on a specific segment, namely, $A_1^o A_2^o$, and we utilize the piece-wise constant curvature approximation (PCCA). In this single segment, the base platform and the moving platform are interconnected by two cables or tendons, specifically designated as ρ_1^j and ρ_1^i, which are positioned on either side of the central spine. Additionally, two springs, each with stiffness coefficients k_1^j and k_1^i", are placed between ($A_1^j A_2^j$) and ($A_1^i A_2^i$), respectively. For subsequent segments $A_2^o A_3^o$, $A_3^o A_4^o$, ..., $A_{n-1}^o A_n^o$, a similar definition will be applicable, with sides remaining the same for each stage, respectively.

The act of contracting the cables leads to angular displacement within the flexible beam of the central spine. This effect is observed in all three segments, consequently causing the mechanism to bend. The cable's length is quantified as $\rho_n^{i/j}$.

3.1. Kinematics Equations of One Segment

In order to determine the locations of the points on the mobile platform, it becomes imperative to investigate the deformation of a beam under torsion. We assume that the distance between A_1^o and A_2^o is h_1 when the mechanism is in its neutral position. Also, A_1^o is the centre point of $A_1^i A_1^j$, where, $A_1^i A_1^o = A_1^o A_1^j = l_1$.

The coordinates of the fixed points are

$$\mathbf{a}_1^j = \begin{bmatrix} -l_1 & 0 \end{bmatrix}^T \quad \mathbf{a}_1^i = \begin{bmatrix} l_1 & 0 \end{bmatrix}^T \tag{1}$$

and in the moving reference frame

$$\mathbf{a}_2^j = \begin{bmatrix} -l_1 & 0 \end{bmatrix}^T \quad \mathbf{a}_2^i = \begin{bmatrix} l_1 & 0 \end{bmatrix}^T \tag{2}$$

where, $\mathbf{a}_n^{i/j}$ is the vector representation of graphical point $A_n^{i/j}$.

During the formulation of the multi-segmented structure, the mechanism's width remained consistent with that shown in Equations (1) and (2). This determination was made after examining the stability between a mechanism with a consistent width and one with a tapering width, as depicted in [24].

To correlate cable tensions and spring forces in one segment with its radius of curvature, we employ a lumped parameter model. In the context of a beam, the springs and cables exert forces on its ends, leading to the generation of a torsional torque:

$$\mathcal{T}_1 = \mathcal{T}_{f_1^j} + \mathcal{T}_{f_1^i} + k_1^j(\rho_1^j - d_1^j)l_2 - k_1^i(\rho_1^i - d_1^i)l_2 \tag{3}$$

where $\mathcal{T}_{f_1^j} = -f_1^j l_2$ and $\mathcal{T}_{f_1^i} = f_1^i l_2$. Equation (4) represents Hooke's law with a rotational spring and the bending moment. In this equation, K_θ stands for the effective bending stiffness (measured in N·m/rad), h_1 signifies the arc length between A_1^o and A_2^o, f_1 and f_2 denote the forces applied by the two cables, and r_1 represents the radius of curvature (as illustrated in Figure 4). In the context of a single section, it can be expressed as follows:

$$h_1/r_1 = \mathcal{T}_1/K_\theta \tag{4}$$

The characterization of the beam can be denoted by its bending radius r_1 and the angle θ_1.

$$r_1 = h_1/\theta_1 \quad \text{and} \quad \theta_1 = \tau_1/K_\theta \tag{5}$$

This definition holds true when we bend in one direction, whether to the left or right, and it enables us to determine the position of A_2^o.
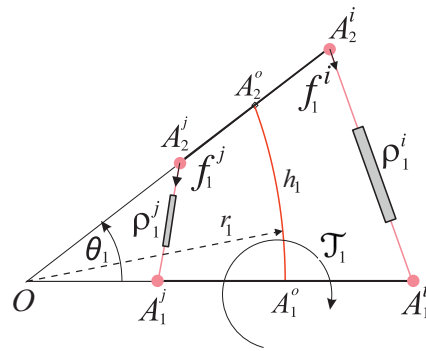
Figure 4. Bending moment equilibrium [22] when two forces f_1 and f_2 are applied to generate the torque $\mathcal{T}_1$.

The segment $(A_2^j A_2^i)$ is normal to the beam at point A_2^o and the coordinates of these points are

$$\mathbf{a_2^o} = \begin{bmatrix} r_1 - r_1 \cos(\theta_1) \\ r_1 \sin(\theta 1) \end{bmatrix} \tag{6}$$

$$\mathbf{a_2^j} = \begin{bmatrix} r_1 - r_1 \cos(\theta 1) - l_2 \cos(\theta 1) \\ R \sin(\theta 1) + l_2 \sin(\theta 1) \end{bmatrix} \tag{7}$$

$$\mathbf{a_2^i} = \begin{bmatrix} r_1 - r_1 \cos(\theta 1) + l_2 \cos(\theta 1) \\ R \sin(\theta 1) - l_2 \sin(\theta 1) \end{bmatrix} \tag{8}$$

The inverse kinematic model for a mechanism featuring a flexible beam can be presented as follows:

$$||\mathbf{a_1^j} - \mathbf{a_2^j}|| = \rho_1^j, \quad ||\mathbf{a_1^i} - \mathbf{a_2^i}|| = \rho_1^i \tag{9}$$

These equations can likewise be represented as functions of the spring lengths; hence,

$$(-l_1 - r_1 + r_1 \cos(\theta 1) - l_2 \cos(\theta_1))^2 + (-r_1 \sin(\theta_1) + l_2 \sin(\theta_1))^2 = (\rho_1^j)^2 \tag{10}$$

$$(l_1 - r_1 + r_1 \cos(\theta_1) + l_2 \cos(\theta_1))^2 + (-r_1 \sin(\theta_1) - l_2 \sin(\theta_1))^2 = (\rho_1^i)^2 \tag{11}$$

Similar to previous assumptions, for other sections, we can write the equations in the same way for the positions of the joints. The inverse kinematic model of the sections is given by

$$||\mathbf{a_{n-1}^j} - \mathbf{a_n^j}|| = \rho_{n-1}^j, \quad ||\mathbf{a_{n-1}^i} - \mathbf{a_n^i}|| = \rho_{n-1}^i, \tag{12}$$

3.2. Force Transmissions between Segments

To determine the position of the mobile platform as a consequence of the application of force in the tendons or cables, it becomes imperative to compute the radius of curvature and the angle of inclination that align with the kinematic model.

The optimization problem $\mathcal{S}$ for a single segment is written using Equation (9), as follows:

$$\mathcal{S} = \text{Minimize}\left((||\mathbf{a_1^j} - \mathbf{a_2^j}|| - \rho_1^j)^2 + (||\mathbf{a_1^i} - \mathbf{a_2^i}|| - \rho_1^i)^2 \right) \tag{13}$$

with $\rho_1^i \geq 0$, $\rho_1^j \geq 0$, $\rho_1^i \leq 3$, $\rho_1^j \leq 3$. This function is generalized for n-segments by summing the squares of the equations associated with each segment.

For each segment, it is necessary to assess the bending moment and its transfer to the preceding one. When $f_n^i > f_n^j$, the beam exhibits a rightward bend. The cables pass through the eyelet, introducing friction denoted as μ. Figure 5 visually illustrates the transmission of forces before and after the cable passes through the eyelets on the mobile platform. The examination of segment stability, while considering cable friction in the eyelets, allows for the derivation of force transmission coefficients [22].
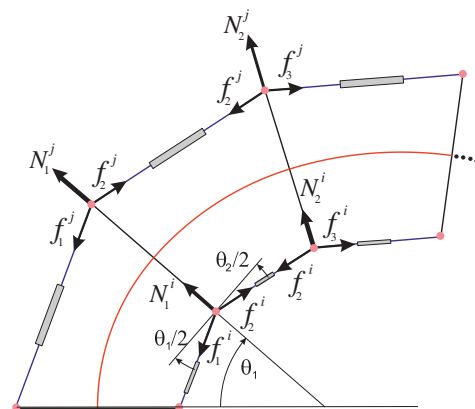
Figure 5. Static equilibrium of three segments.

For actuators on the right side of the central axis, the tensions in the cables reduce from the base to the end as

$$\frac{f_{n+1}^i}{f_n^i} = \left(\frac{1 - \mu \sin(\theta_1/2)}{1 + \mu \sin(\theta_1/2)}\right) \tag{14}$$

For actuators on the left side of the central axis, the tensions in the cables increase from the base to the end as

$$\frac{f_{n+1}^j}{f_n^j} = \left(\frac{1 + \mu \sin(\theta_1/2)}{1 - \mu \sin(\theta_1/2)}\right) \tag{15}$$

3.3. Motion Simulations

In this section, we suggest conducting a simulation study using the SIROPA library [25] within the MAPLE software (Version 2023, Maplesoft, Waterloo, ON, Canada). The primary aim of this investigation is to examine the behavioural characteristics of the mechanism. It is crucial to emphasize that, at this juncture, specific model parameters are undefined, requiring a thorough selection of materials and a comprehensive comprehension of the system's workspace.

To visually illustrate the bending motion of the mechanism in response to different force magnitudes, we refer to Figure 6, where red curve depict the central spine and blue lines depict the tendons/cable. This figure provides a visual representation of the bending motion, as it responds to force magnitudes ranging from $f_1 - f_2 = 0 + \epsilon$ to 17 N. The range set between 0 and 17 N was meticulously in accordance with the study's constraints. This range encompasses the utmost extent of bending achievable for the mechanism outlined in the article under the considered limitations. The inclusion of a small offset symbolized as ϵ, holds great importance in preventing a situation in which the radius of curvature tends to infinity, as in practicality, the equality of both forces is impossible.

Nevertheless, the introduction of length restrictions on the springs, each featuring a spring constant of 100 N/m, gives rise to a distinct set of challenges related to achieving the intended range of motion. The system reaches an extreme configuration in various scenarios: when one of the springs reaches its minimum length, experiences full compression, or when the cable aligns tangentially with the curved configuration.

To tackle these challenges, we resolve this matter by imposing constraints on the spring lengths, restricting them to only 40% of their initial length in the home pose. This particular modification results in a maximum bending angle of around 1.15 radians ($\approx$130°). This angular parameter serves as a crucial metric in assessing the performance of the mechanism under these specific constraints, providing valuable insights into its operational capabilities.
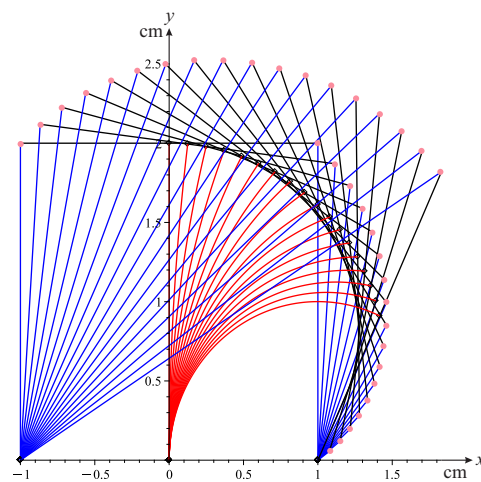
Figure 6. Simulation of the bending of one segment with $l_1 = l_2 = 1$ cm and $h_1 = 2$ cm.

In our simulation, we leverage the power of inverse kinematics to solve for the parameters outlined in Equations (9) and (12), employing the same optimization algorithm as used for a single segment. Notably, in the absence of friction, our simulation of the mechanism's flexion yields a seamless and continuous curve across each segment, as vividly demonstrated in Figure 7 (left). To carry out this optimization and determine the beam's curvature, we harnessed the capabilities of the MAPLE software (Version 2023, Maplesoft, Waterloo, ON, Canada) optimization package, utilizing cable forces and spring tensions as crucial inputs.
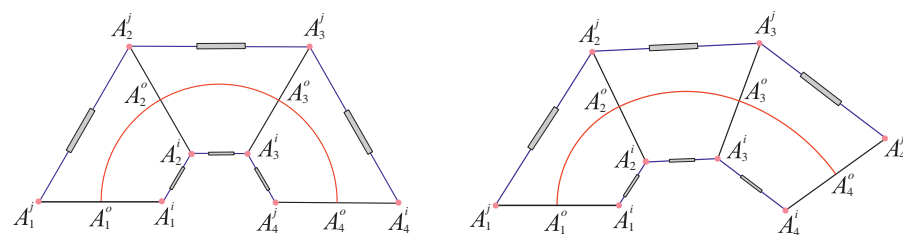
Figure 7. Simulation of bending for three segments with $\mu = 0$ (**left**) and $\mu = 0.2$ (**right**).

When we introduce friction into the system, a notable change occurs in the tension levels of the two cables within each segment. This alteration has a direct impact on the curvature, which is visually evident in Figure 7 (right). It is essential to acknowledge that our model, while informative, maintains a simplification in which it assumes a consistent curvature angle across all segments.

Implementing a tensegrity mechanism for the creation of a flexible stapler in the confined and intricate workspace of a patient's body brings about a reduction in the cross-sectional dimensions of each individual segment. However, this design presents a significant challenge. The slender cross-section width causes the folding beam to intersect with the actuating cables, even at slight deviation angles, resulting in an enlarged radius of curvature, as illustrated in Figure 8.

To ensure unimpeded access to the patient's workspace, it becomes imperative to incorporate an auxiliary joint, which resembles a wrist, before reaching the stapler section. Alternatively, one may address this issue by increasing the number of segments. However, it is crucial to consider that augmenting the segment count may potentially introduce heightened friction between the cables and the eyelets through which they pass. Careful engineering consideration is necessary to strike a balance between these design factors.
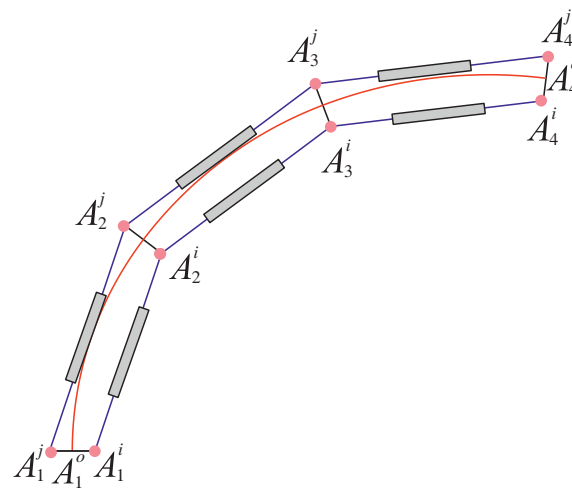
Figure 8. Bending singularity occurring due to reduced cross-section

4. Stapler Design and Prototype

In this section, we are interested in the intricate process of designing and bringing to life the kinematic equations that were introduced in the preceding segment. Building upon a robust mathematical model, extensive simulations, and a thorough examination of potential singularities, we have meticulously crafted a sophisticated multi-segmented mechanism with a total of ten segments (referred to as $n = 10$). This innovative creation, depicted in Figure 9, takes the form of a slotted beam-type flexible jaw mechanism, which is uniquely endowed with the ability to bend within a single plane, aligning perfectly with the plane in which staple insertion occurs.
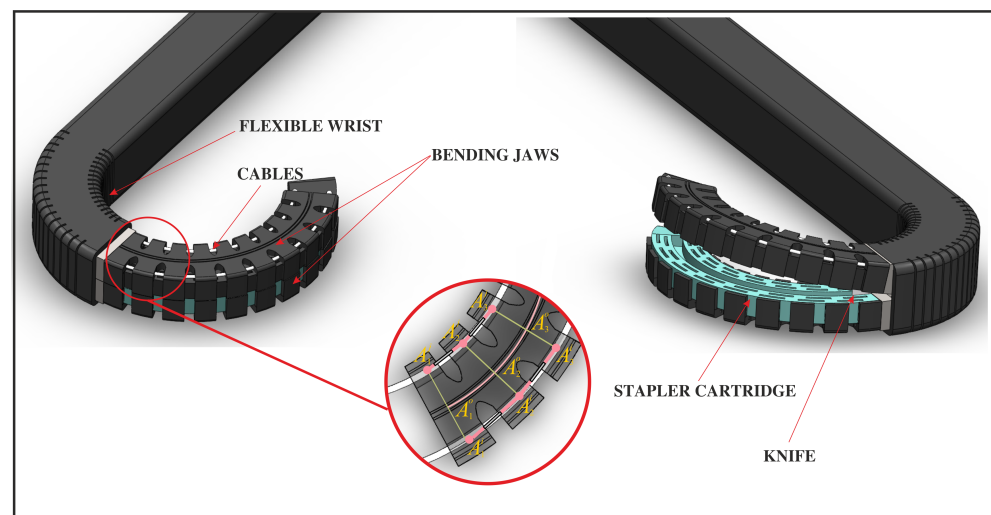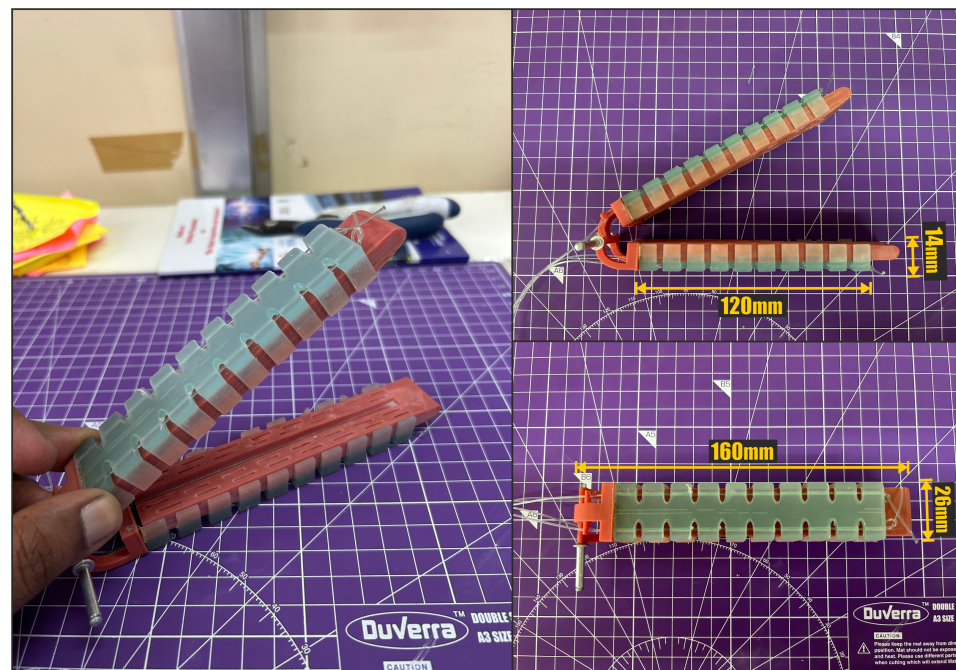

Figure 9. FLexible surgical stapler design

To further elevate its maneuverability and versatility, our design incorporates a compound flexible wrist, seamlessly working in conjunction with the flexible jaws. As an added feature, we've also integrated a knife into the stapler cartridge, strategically positioned to expedite tissue separation once the staple pins have been successfully deployed. This comprehensive design approach represents a significant step forward in the field, optimizing the performance and functionality of this medical tool for improved patient outcomes.

After completing the CAD modeling and rigorous simulations, we moved on to the next phase, in which we brought our vision to life through the creation of a scaled-up prototype. This prototype, enlarged by 200% along the centroid, represents the stapler jaws and was fabricated using cutting-edge 3D printing technology (see Figure 10). Specifically, we employed a Stereo-lithography Apparatus (SLA)-type 3D printer, which utilizes a

liquid polymer resin as its foundational material and employs UV radiation to solidify the intended pattern. For this particular prototype, we selected "MONOCURE 3D FLEX 100" resin due to its high flexibility and structural weaknesses. To enhance the overall rigidity of the 3D printed part, we added a small amount of "ANYCUBIC 3D printing UV sensitive (Aqua)" resin, known for producing hard and rigid 3D-printed components. The mixing ratio for these resins was 80–20%, with MONOCURE flexible resin making up 80% and ANYCUBIC (Aqua) accounting for the remaining 20%. The curing process took approximately 120 min, resulting in a composite material with distinctive properties, as outlined in Table 1.

Table 1. Material properties of 3D-printed parts.

Properties	Values
Density (ρ)	1290.57 kg/m^3
Ultimate Tensile Strength (UTS)	1.6416 MPa
Poisson's ratio (ν)	0.35
Young's Modulus (E)	4.83 MPa

Figure 10. The 3D-printed prototype of flexible surgical stapler.

Following the fabrication of the prototype, we conducted a series of rigorous bending tests to evaluate its mechanical performance under varying force levels. The testing apparatus employed a pulley system, with weights attached to one of the cables incorporated into the 3D-printed prototype. To measure the prototype's flexibility and resilience, we marked its centerline tip and observed only the tip's movement during bending. The resulting bending motion was meticulously traced on a sheet of plotting paper to map the trajectory of the tip. Various weights, ranging from 100 g to 1500 g, were incrementally applied as depicted in Figure 11, and the resultant displacement of the prototype's tip in both the X and Y directions, along with its angular deflection (α) relative to the central axis at the neutral position, were meticulously recorded and detailed in Table 2 and depicted in Figure 12. These tests provide critical insights into the mechanical behavior and performance of our prototype.
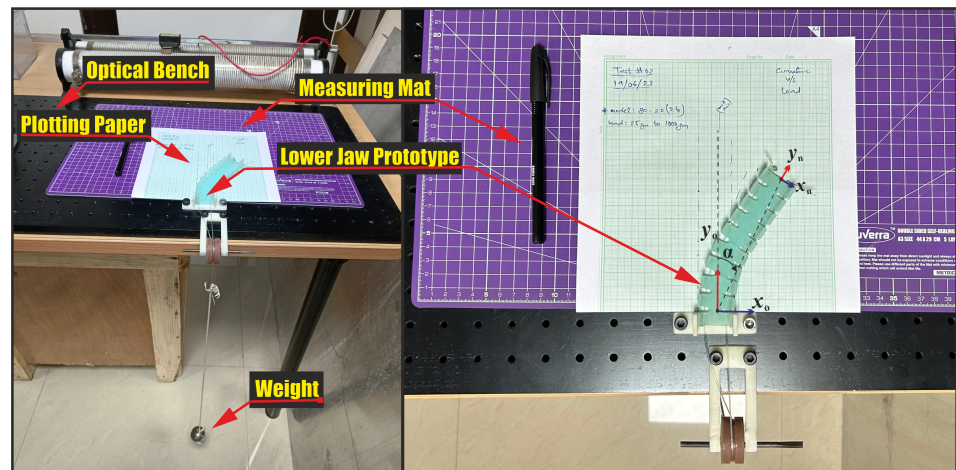
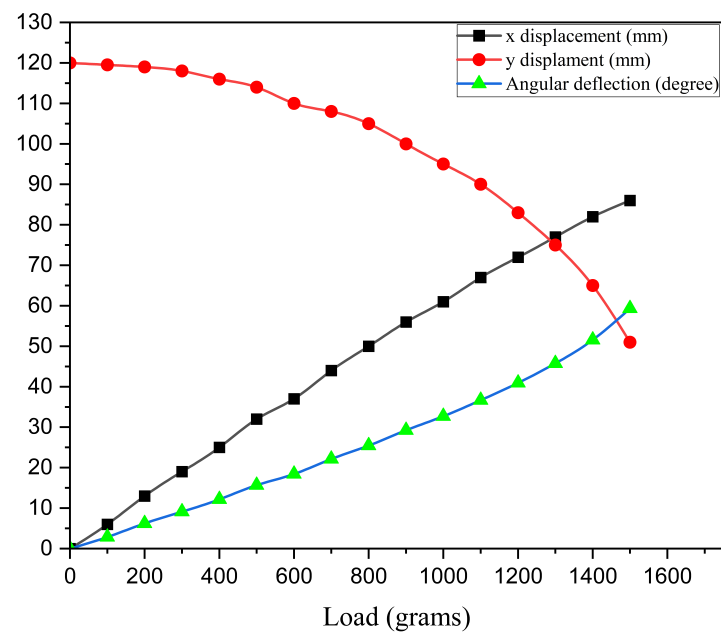**Figure 11.** Testing of 3D-printed prototype of lower Jaw.

Figure 12. Plot of *x* displacement, *y* displacement and angular deflection of prototype tip (α) vs. load applied, as presented in Table 2.

Table 2. Table for load v/s deflection of the tip of the 3D-printed lower jaw prototype.

Sl. No.	Load (g)	X Displacement (mm)	Y Displacement (mm)	Angular Deflection (α) (deg)
1	0	0	120	0
2	100	6	119.5	2.86
3	200	13	119	6.23
4	300	19	118	9.14
5	400	25	116	12.16
6	500	32	114	15.67
7	600	37	110	18.43
8	700	44	108	22.16
9	800	50	105	25.46
10	900	56	100	29.24
11	1000	61	95	32.70
12	1100	67	90	36.66

Table 2. *Cont.*

Sl. No.	Load (g)	X Displacement (mm)	Y Displacement (mm)	Angular Deflection (α) (deg)
13	1200	72	83	40.94
14	1300	77	75	45.75
15	1400	82	65	51.59
16	1500	86	51	59.33

5. Conclusions and Future Work

In this article, we have investigated a flexible mechanism designed for application within a stapler during laparoscopic total mesorectal excision procedures for rectal cancer and other colorectal interventions. These procedures introduce challenges for traditional tools due to constrained accessibility and the limited space available for manoeuvring such stapler tools. The mechanism comprises three stacked tensegrity structures, which consist of rigid bodies, linear springs, actuation cables, and a flexible beam. The dimensions of the stapler are determined based on various factors, including patient anatomy and the constraints imposed by laparoscopy. Currently, patient scans are under analysis to define the surgical workspace.

We employed a lumped parameter model to analyze the mechanism, factoring in the presence or absence of friction in each rigid segment's eyelet. Our findings underscore the impact of friction on curvature radius, necessitating precise analysis. Ongoing research focuses on understanding the friction between the mobile platform eyelets and cables as we add more sections, anticipating increased overall friction that may potentially affect curvature beyond expectations.

The materials used are under evaluation, especially the sheathing covering the mechanism. The stapler's outer skin, which is made of elastomer, doubles as a spring for sealing and medical equipment suitability. This research signifies a vital step in advancing surgical stapler technology for complex procedures, enabling more effective and precise surgeries in challenging anatomical regions.

Our future goal is to gather more data and enhance data analysis, constructing a three-dimensional workspace representation. This will facilitate better analysis of the surgical stapler design and identification of engineering and anatomical constraints for improved problem-solving and design optimization.

References

1. Gaidry, A.D.; Tremblay, L.; Nakayama, D.; Ignacio, R.C. The History of Surgical Staplers: A Combination of Hungarian, Russian, and American Innovation. *Am. Surg.* **2019**, *85*, 563–566. [CrossRef]
2. Robicsek, F.; Konstantinov, I. Hümer Hültl: The father of the surgical stapler. *J. Med Biogr.* **2001**, *9*, 16–19. [CrossRef]
3. Akopov, A.; Artioukh, D.Y.; Molnar, T.F. Surgical Staplers: The History of Conception and Adoption. *Ann. Thorac. Surg.* **2021**, *112*, 1716–1721. [CrossRef]
4. Demertzis, S.; Beslac, O.; Mettler, D.; Zalokar, D.; Spangler, T.; Hausen, B.; Swanstrom, L. Beyond the B: A new concept of the surgical staple enabling miniature staplers. *Surg. Endosc.* **2015**, *29*, 3674–3684. [CrossRef]
5. Kostrzewski, S.; Aranyi, E.; Scirica, P. In-Situ Loaded Stapler. US Patent 9364217B2, 14 June 2016.
6. McGuire, J.; Wright, I.; Leverment, J. Surgical staplers: A review. *J. R. Coll. Surg. Edinb.* **1997**, *42*, 1–9.
7. Adams, R.D.; Main, L.O.; Swaffar, S.E.; Pugsley, C.H., Jr.; Gordon, D.P. Endoscopc Stapler. US Patent 6302311, 16 October 2001.
8. Tobias, K.M. Surgical Stapling Devices in Veterinary Medicine: A Review. *Vet. Surg.* **2007**, *36*, 341–349. [CrossRef]
9. Schemmer, P.; Friess, H.; Dervenis, C.; Schmidt, J.; Weitz, J.; Uhl, W.; Büchler, M.W. The Use of Endo-GIA Vascular Staplers in Liver Surgery and Their Potential Benefit: A Review. *Dig. Surg.* **2007**, *24*, 300–305. [CrossRef]
10. Holzmacher, J.L.; Luka, S.; Aziz, M.; Amdur, R.L.; Agarwal, S.; Obias, V. The use of robotic and laparoscopic surgical stapling devices during minimally invasive colon and rectal surgery: A comparison. *J. Laparoendosc. Adv. Surg. Tech.* **2017**, *27*, 151–155. [CrossRef]
11. Bolanos, H.; Norwalk, E.; Sherts, C.R.; Southport; Pelletier, A.T.; Wallingford. Endoscopic Stapler. US Patent 690269, 5 November 1997.
12. Milliman, K.L.; Bethel; Viola, F.J.; Hook, S.; Orban, J.; Norwalk; Lehn, R.F.; Stratford. Surgical Stapling Apparatus. US Patent 586531, 2 February 1999.
13. Ema, T. The experience of using Endo GIA Radial Reload with Tri-Staple Technology for various lung surgery. *J. Thorac. Dis.* **2014**, *6*, 1482–1484. [CrossRef]
14. Rivadeneira, D.E.; Verdeja, J.C.; Sonoda, T. Improved access and visibility during stapling of the ultra-low rectum: A comparative human cadaver study between two curved staplers. *Ann. Surg. Innov. Res.* **2012**, *6*, 11. [CrossRef]
15. Ruffo, G.; Sartori, A.; Crippa, S.; Partelli, S.; Barugola, G.; Manzoni, A.; Steinasserer, M.; Minelli, L.; Falconi, M. Laparoscopic rectal resection for severe endometriosis of the mid and low rectum: Technique and operative results. *Surg. Endosc.* **2012**, *26*, 1035–1040. [CrossRef]
16. de Calan, L.; Gayet, B.; Bourlier, P.; Perniceni, T. Chirurgie du cancer du rectum par laparotomie et par laparoscopie. *EMC Chir.* **2004**, *1*, 231–274. [CrossRef]
17. Furet, M.; Lettl, M.; Wenger, P. Kinematic Analysis of Planar Tensegrity 2-X Manipulators. In Proceedings of the International Symposium on Advances in Robot Kinematics, Bologna, Italy, 1–5 July 2018; Springer: Berlin/Heidelberg, Germany, 2018; Volume 8, pp. 153–160. [CrossRef]
18. Chekan, E.; Whelan, R. Surgical stapling device-tissue interactions: What surgeons need to know to improve patient outcomes. *Med Devices Evid. Res.* **2014**, *7*, 305. [CrossRef]
19. Ghosh, S.; More, N.; Kapusetti, G. Surgical staples: Current state-of-the-art and future prospective. *Med. Nov. Technol. Devices* **2022**, *16*, 100166. [CrossRef]
20. Khanzode, D.; Jha, R.; Thomieres, A.; Duchalais, E.; Chablat, D. Design of a surgical stapler for laparoscopic colectomy. In Proceedings of the International Workshop on Medical and Service Robots, Craiova, Romania, 7–10 June 2023; Springer: Berlin/Heidelberg, Germany, 2023; pp. 71–80. [CrossRef]
21. Gravagne, I.; Rahn, C.; Walker, I. Large deflection dynamics and control for planar continuum robots. *IEEE/ASME Trans. Mechatron.* **2003**, *8*, 299–307. [CrossRef]
22. Kato, T.; Okumura, I.; Song, S.E.; Golby, A.J.; Hata, N. Tendon-Driven Continuum Robot for Endoscopic Surgery: Preclinical Development and Validation of a Tension Propagation Model. *IEEE/ASME Trans. Mechatron.* **2015**, *20*, 2252–2263. [CrossRef]
23. Khanzode, D.; Jha, R.; Chablat, D.; Duchalais, E. Stapler design with stacked tensegrity mechanisms for surgical procedures. In Proceedings of the International Design Engineering Technical Conferences and Computers and Information in Engineering Conference, St. Louis, MI, USA, 14–17 August 2022; American Society of Mechanical Engineers: New York, NY, USA, 2022; Volume 86281, p. V007T07A037. [CrossRef]
24. Khanzode, D.; Jha, R.; Duchalais, E.; Chablat, D. Stacked Tensegrity Mechanism for Medical Application. In Proceedings of the International Symposium on Advances in Robot Kinematics, Bilbao, Spain, 26–30 June 2022; Springer: Berlin/Heidelberg, Germany, 2022; pp. 139–148.
25. Jha, R.; Chablat, D.; Baron, L.; Rouillier, F.; Moroz, G. Workspace, joint space and singularities of a family of delta-like robot. *Mech. Mach. Theory* **2018**, *127*, 73–95. [CrossRef]